نشریه ژئومکانیک و ژئوانرژی (ژئومکانیک نفت)

GEOMECHANICS and GEOENERGY JOURNAL (GGJ)

Original article

Enhancing Oil Field Characterization Through Seismic Crosswell Tomography: A Comparative Study of Structured vs. Unstructured Meshing for Improved Inversion Accuracy

Amir Yazdanpanah[1], Maysam Abedi[1*]

1- School of Mining Engineering, College of Engineering, University of Tehran, Tehran, Iran.

Received: 2025/8/28; Accepted: 2025/12/23

DOI: 10.22107/ggj.2025.539990.1256

Keywords

SeismicCrosswell Tomography,
Oil Field Characterization,
Structured Mesh,
Unstructured Mesh,
Velocity Inversion,
Subsurface Anomalies.

Abstract

Seismic crosswell tomography is recognized as a robust method for characterizing subsurface structures in oil field exploration. In this study, the effectiveness of structured and unstructured meshing strategies is evaluated for inverting seismic crosswell tomography data to enhance subsurface velocity imaging. A synthetic layered model, representative of oil field geology and incorporating gas, oil, and saline water anomalies with distinct velocity contrasts, is utilized to simulate wave propagation and reconstruct velocity distributions through a finite element-based approach. Structured meshing is found to provide computational stability and uniform resolution, suitable for simpler geological settings, though artifacts may be introduced in complex anomaly regions. In contrast, unstructured meshing is adapted to geological heterogeneity, thereby improving the resolution of anomaly-related velocity contrasts, albeit with increased computational requirements. Comparative analysis of velocity reconstructions, misfit distributions, and ray path coverage is conducted to elucidate the trade-offs between these meshing strategies, informing optimal mesh design for accurate subsurface characterization. The findings derived from this research significantly enhance the field of seismic crosswell tomography, particularly in the context of oil field investigations. This study is limited to synthetic 2D modeling, and the absence of field validation and 3D modeling warrants further investigation to confirm real-world applicability. By providing valuable insights into the intricacies of mesh optimization, this study paves the way for achieving exceptionally high-resolution geophysical imaging of subsurface hydrocarbon anomalies.

1. Introduction

Seismic crosswell tomography enables high-resolution imaging of subsurface structures in oil field exploration by placing sources and receivers in boreholes to generate detailed velocity models [1]. Meshing strategies in the inversion process critically influence model accuracy, impacting reservoir management success.

Crosswell tomography has advanced subsurface imaging, mapping interwell lithology for enhanced oil recovery [2]. Waveform tomography addresses anisotropy in layered sediments, yielding high-resolution velocity models [3]. Hybrid computational methods, combining Radon-transform back-projection and eikonal solvers, improve initial models for full waveform inversion [4]. Frequency-dependent traveltime tomography aligns with sonic logs, validating its utility in complex settings [5]. Incorporating prior velocity data enhances accuracy in heterogeneous environments [6]. Crosswell reflection imaging outperforms vertical seismic profiling for small-scale features [7].

Complex wavefield challenges in reservoir monitoring are addressed by inverse Gaussian-beam imaging, improving transverse resolution in

*Corresponding author: maysamabedi@ut.ac.ir

structural traps [8]. The inverse Fresnel beam method optimizes velocity models via first-arrival tomography [9]. Frequency-domain reverse time migration reduces artifacts, enhancing image quality [10]. Q-compensated migration counteracts attenuation, clarifying reservoir boundaries [11]. Illumination limitations affect resolution, introducing artifacts in slowness fields [12]. Shear wave splitting estimates anisotropy, aiding hydrocarbon detection [13]. Deep reservoir imaging confirms pinchout zones and continuity [14].

Complementary methods enhance crosswell tomography. Electromagnetic (EM) tomography maps hydrocarbon saturations in fractured reservoirs using Archie's law [15]. Signal processing improves EM imaging accuracy over large well separations [16]. Seismic-EM integration with ensemble-Kalman matching improves permeability estimation [17]. Time-lapse 3D resistivity monitors CO_2 flow, reducing artifacts via focused inversion [18]. Superparamagnetic nanoparticles enhance flood imaging [19]. Combined seismic-EM tomography monitors CO_2 in aquifers, recovering petrophysical properties [20]. In urban settings, resistivity and seismic tomography detect karst caves, optimizing efficiency [21].

Crosswell tomography supports hydraulic fracturing and CO_2 sequestration monitoring. Repeat tomography evaluates fracture creation in shale reservoirs, detecting velocity changes [22]. Shear-wave analysis identifies fracture azimuth and intensity [23]. Virtual horizontal tomography monitors CO_2 plume migration [24]. Tube wave characterization enhances velocity estimation and survey repeatability [25]. 4D resistivity tracks oil-water fronts [26]. Crosswell electromagnetics monitors CO_2 plumes in conductive aquifers [27]. Piezoelectric sources and beamforming improve velocity images in noisy environments [28]. Cross-validation ensures reliable inversions [29].

Meshing strategies in finite element-based crosswell inversion remain underexplored. Structured versus unstructured meshing impacts accuracy in handling interwell heterogeneity, with computational cost and resolution challenges requiring systematic evaluation [30]. Finite element meshing balances computational efficiency and geological representation. Unstructured meshes, using triangles or tetrahedra, model complex velocity fields with reduced memory [31]. Structured meshes suit resolved synthetic seismograms but struggle with complex geometries, where unstructured meshes excel [32]. SimPEG and pyGIMLi support finite element-based tomography [33, 34]. SimPEG offers modular mimetic discretizations for flexible inversion. pyGIMLi excels in unstructured mesh handling and coupled inversions, suitable for high-resolution crosswell imaging. This study uses pyGIMLi for its robust traveltime tomograp
hy capabilities.

In this study, a synthetic deep layered model is simulated using unstructured meshing, implemented through the pyGIMLi library, version 1.4.3. Forward and inverse modeling processes are undertaken on a laptop equipped with 16GB RAM and a 12th Gen Intel® Core™ i7-1255U CPU.

2. Methodology

A finite element-based crosswell traveltime tomography model is established to assess the performance of structured and unstructured meshing strategies in reconstructing subsurface velocity distributions within a synthetic layered oil field framework. Seismic wave propagation is simulated across a 2D domain, incorporating two boreholes equipped with sensors and a layered velocity structure, augmented by gas, oil, and saline water anomalies with velocity contrasts. Traveltime tomography, governed by eikonal equations and solved through a very high quality unstructured mesh, is employed to generate high-resolution velocity models for both meshing approaches.

2.1. Forward Modeling

Synthetic traveltime data are computed for a 2D seismic crosswell tomography model to assess the performance of meshing strategies. Traveltime calculations are governed by the Eikonal equation [35]:

$$|\nabla T(x,z)| = \frac{1}{V(x,z)} \quad (1)$$

where $T(x,z)$ denotes first-arrival traveltime at position (x,z), and $V(x,z)$ is the seismic velocity. The forward operator $F_j\,[m]$ maps the velocity model m to synthetic traveltime data d_j^{obs}, incorporating noise n_j (0.1% relative, 10^{-5} absolute) for 1521 (39×39) source-receiver pairs [36]:

$$F_j\,[m] = d_j^{obs} \equiv d_j + n_j\,, \quad j = 1, \dots, N \tag{2}$$

The quality of the unstructured triangular mesh used for forward and inverse modeling is assessed to ensure accurate representation of the subsurface. The mesh, constructed via Delaunay triangulation (DT), assumes constant properties within each triangular cell. Mesh quality is evaluated using the quality parameter η, defined as:

$$\eta = \frac{4\sqrt{3}a}{l_1^2 + l_2^2 + l_3^2} \tag{3}$$

Here, a is the area of a triangle, l_1, l_2, l_3 are its edge lengths, and the factor $4\sqrt{3}$ normalizes the quality of an equilateral triangle to $\eta = 1$. This metric ensures that the mesh effectively captures geological interfaces, with its quality visualized in the study. It is conducted to confirm suitability for finite element-based traveltime calculations [37].

2.2. Inverse Modeling

The inverse problem in crosswell traveltime tomography seeks to reconstruct the subsurface velocity distribution from observed traveltime data. Within the geometric optics approximation, the traveltime τ_i of a seismic ray from source to receiver is related to the slowness ($s(x,z) = \frac{1}{V(x,z)}$), where $V(x,z)$ is the seismic velocity in the 2D domain. The traveltime is expressed as [38]:

$$\tau_i = \int_{\Gamma_i} s(x,z)ds \tag{4}$$

where Γ_i represents the raypath between the source and the i-th receiver, and ds is the differential arc length along the ray. This relationship is nonlinear because the raypath Γ_i depends on the slowness $s(x,z)$. To linearize the problem, Fermat's principle is employed, stating that traveltime is stationary with respect to small raypath perturbations. For a background slowness model $S_b(x,z)$ perturbed slightly to $s(x,z) = s_b(x,z) + \delta s(x,z)$, the traveltime variation is approximated as [38]:

$$\tau_i \approx \tau_i(s_b) + \int_{L(s_b)} \delta s(x,z)ds \tag{5}$$

Here, $\tau_i(s_b)$ is the traveltime along the raypath $L(s_b)$, a straight line in a homogeneous background medium, and $\delta s(x,z)$ is the slowness perturbation. The subsurface is discretized into L cells using either a structured grid or an unstructured triangular mesh, with constant slowness s_L per cell. The model parameters form a vector:

$$m = s_1, s_2, \dots, s_L \tag{6}$$

The observed data are represented as a vector of first-arrival traveltimes for N source-receiver pairs:

$$d = \tau_1, \tau_2, \dots, \tau_N \tag{7}$$

This results in a linear system for the slowness distribution:

$$d = f(m) = Am \tag{8}$$

where $A = [A_{ij}]$ is the sensitivity matrix, with A_{ij} denoting the distance traveled by the i-th ray in the j-th cell. This system is solved using the pyGIMLi library, with regularization applied to ensure stable velocity model reconstruction.

The ill-posed inverse problem in crosswell traveltime tomography is stabilized through zero-order Tikhonov regularization, where the L2-norm of the slowness model is penalized to address non-uniqueness and sensitivity to noise. The objective function minimized during inversion is expressed as [39]:

$$\Phi(m) = \left\| W_d\big(d - f(m)\big) \right\|_2^2 + \lambda \| W_m(m - m_0) \|_2^2 \tag{9}$$

Here, W_d is the data weighting matrix accounting for measurement uncertainties, d represents observed traveltime data, $f(m)$ denotes the forward model mapping slowness m to predicted traveltimes, λ controls the regularization strength to balance data misfit and model smoothness. Also, W_m is the model weighting matrix enforcing spatial smoothness across the 2D domain, and m_0 is a predefined reference model. Isotropic weighting is applied with a vertical weighting factor of 1.0 it ensures uniform regularization without directional bias. The solution to the above linear inverse problem is obtained by minimizing Equation 9, yielding the regularized slowness model:

$$m = (A^T W_d^T W_d A + \lambda W_m^T W_m)^{-1} A^T W_d^T W_d d + \lambda W_m^T W_m m_0 \tag{10}$$

In this expression, A^T denotes the transpose of the sensitivity matrix. W_d^T is the transpose of the data weighting matrix, and λ controls the regularization strength, set to 1000 in this study. This solution is computed iteratively using the conjugate gradient method, leveraging the sparsity of A to achieve computational efficiency for both mesh types. It is important to state that the sensitivity matrix A is constructed differently for structured (grid-based) and unstructured (triangular) meshes, affecting computational efficiency.

The subsurface velocity model is iteratively refined during inversion by updating the current model m_k with a correction vector Δm, yielding the updated model. Under the straight-ray assumption, the sensitivity matrix A is considered linear; however, the actual raypath is influenced by the underlying velocity structure. In cases where there are sharp variations in velocity, the rays will follow curved trajectories from the source to the receiver. This curvature indicates that the sensitivity matrix becomes non-linear, necessitating the use of a Jacobian matrix J to accurately represent the relationship. At each iteration k, the sensitivity of the modeled data to changes in model parameters is quantified through the computation of the Jacobian matrix J. These relationships are expressed mathematically as follows:

$$\Delta m = (J^T W_d^T W_d J + \lambda W_m^T W_m)^{-1} J^T W_d^T W_d \big(d - J(m)\big) - \lambda W_m^T W_m (m - m_0) \quad \textbf{(11)}$$

$$m_{k+1} = m_k + \Delta m \quad \textbf{(12)}$$

$$J_{i,j} = \partial f_i / \partial m_i \quad \textbf{(13)}$$

The relative Root Mean Square Error (RMSE) quantifies inversion accuracy in seismic crosswell traveltime tomography by measuring the misfit between observed and predicted traveltime data. For N observations, the observed traveltimes d_i are compared to predicted traveltimes $f_i(m)$, computed from the inverted velocity model. The RMSE error is calculated as below, where i denotes each traveltime observation. This metric provides a direct measure of model fidelity, complementing other accuracy indicators.

$$RMSE(\%) = \sqrt{1/N \sum_{i=1}^{N} \left(\frac{d_i - f_i(m)}{d_i}\right)^2} \times 100 \quad \textbf{(14)}$$

The χ_N^2 statistic is employed to assess the goodness of fit between observed and predicted traveltime data, quantifying the extent to which the inverted model reproduces the measurements relative to data uncertainties. It is defined as [36]:

$$\chi_N^2 = \sum_{i=1}^{N} \left(\frac{d_i - f(m)_i}{\sigma_i}\right)^2 \quad \textbf{(15)}$$

where d_i is the i-th observed traveltime, $f(m)_i$ is the predicted traveltime, σ_i is the standard error of the i-th datum, and N is the number of data points (1521 in this study). Also, N is considered as the degree of freedom of the χ^2parameter. In the pyGIMLi implementation, the χ_N^2 is reported to normalize the misfit by the number of data points, providing a per-datum measure of model accuracy. A reduced χ_N^2 value close to 1 indicates that the residuals are consistent with the specified data uncertainties, ensuring a reliable velocity model .

The inversion process monitors the reduction in the objective function, denoted as $d\varphi$, to evaluate convergence. This parameter represents the change in the objective function $\Phi(m)$ between consecutive iterations, reflecting improvements in the model fit to the data. A decreasing $d\varphi$ indicates that the iterative updates, guided by the line search strategy, are effectively minimizing the combined data misfit and regularization terms. This metric is critical for determining when the inversion has achieved a stable and accurate velocity model for both structured and unstructured meshes.

3. Crosswell Traveltime Tomography Simulation

Simulations of crosswell traveltime tomography are conducted to evaluate structured and unstructured meshing strategies for reconstructing subsurface velocity distributions within a synthetic layered oil field framework. A 1000 m × 2000 m domain is modeled, featuring two boreholes 1000 m apart, each equipped with 39 sensors spaced at 50 m intervals from 50 to 1950 m depth. Synthetic traveltime data for 1521 source-receiver pairs are generated with realistic noise levels (0.1% relative, 10^{-5} s absolute) to emulate field measurements. The survey layout, including borehole and sensor positions, is illustrated in Fig. 1, providing a clear representation of the acquisition geometry.

The subsurface model, detailed in Table 1, comprises four layers representing typical oil field formations, with anomalies introducing localized velocity perturbations. These simulations enable a controlled evaluation of meshing strategies, facilitating comparison of velocity reconstruction capabilities. By benchmarking against theoretical expectations, the approach enhances understanding of subsurface imaging, supporting robust geophysical methods for oil field characterization.

Table.1. Geophysical Properties of the Seismic Crosswell Tomography Model.

Layer/Anomaly	**Subsurface Material**	**Thickness/Extending (m)**	**V_p (m/s)**
Layer 1	Shale and Marl	200	2000
Layer 2	Limestone and Dolomite	1200	3600
Layer 3	Shale	100	2100
Layer 4	Limestone	500	3800
Gas	Gas	Distance =300 to 700, Depth =-900 to -800	2600
Oil	Oil	Distance =250 to 750, Depth =-1000 to -900	2800
Saline Water	Saline Water	Distance =200 to 800, Depth =-1100 to -1000	3000

The forward model geometry is visualized to confirm the suitability of the computational domain for finite element modeling. Fig. 2a depicts the geometric representation of unstructured triangular mesh used for forward modeling, with an average cell area of 50 m² and 62,138 cells, designed to capture geological interfaces accurately, as specified in Table 2. This visualization ensures the mesh aligns with the intended subsurface structure, supporting robust wave propagation simulations.

Table. 2. Meshing Parameters.

Mesh Type	**Forward Mesh**	**Inversion Structured Mesh**	**Inversion Unstructured Mesh**
Cell Type	Triangular	Rectangular	Triangular
Cell Count	62,287	6612	6618
Node Count	31,419	6785	3403
Runtime (s)	445.18	8417.34	3555.01
Refinement	-	0.35	-
Quality	20	-	20
Area (m^2)	50	17.5×17.5	468.3

The subsurface model's velocity distribution is presented to highlight its layered structure and embedded anomalies. Fig 2b illustrates the four-layer model, augmented by gas (2600 m/s), oil (2800 m/s), and saline water (3000 m/s) anomalies located between distance = 250 –800 m and depth = -1100 to -800 m. This Fig provides a reference for evaluating inversion outcomes, emphasizing the challenge of resolving localized velocity contrasts.

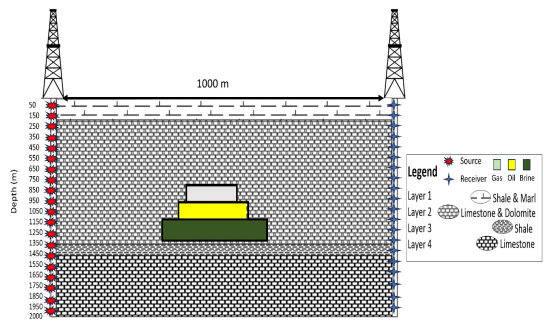

Fig. 1. Overview of the crosswell tomography survlayout, illustrating the spatial arrangement of boreholes and sensor arrays within the study domain.

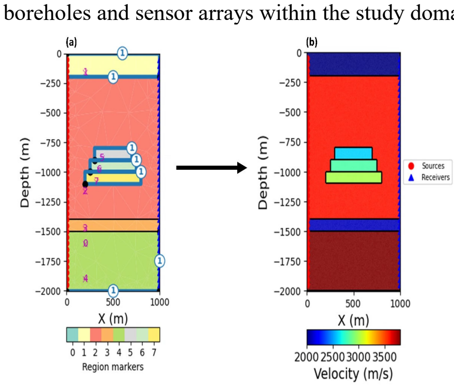

Fig. 2. (a) Geometric representation of the forward model mesh, highlighting the layered subsurface structure and anomalies within the crosswell survey domain, with sensor placements indicated; (b) Velocity distribution across the same mesh, illustrating the assigned velocity values corresponding to geological layers, providing the initial model for inversion analysis.

The forward mesh, used for traveltime data generation, is presented in Fig. 3a, showcasing its finer resolution (62,138 cells) to ensure accurate calculations, as detailed in Table 2. This Fig confirms the mesh's suitability for forward modeling, supporting precise simulation of wave propagation across the domain.

For inversion, structured and unstructured meshes are employed, with an initial model constructed from borehole well logs at x=0 and x=1000 m, reflecting layered velocities (2000, 3600, 2100, 3800 m/s) but excluding anomalies due to the absence of central region data. This approach mimics realistic scenarios where only borehole data inform the layer structure. The structured inversion mesh, visualized in Fig. 3b, consists of 6612 rectangular cells (17.5×17.5 m²), offering uniform resolution and computational stability.

The unstructured inversion mesh is examined to highlight its adaptability to subsurface heterogeneities. Fig. 3c illustrates this mesh, with 6620 triangular cells (average area 468.3 m²), designed to conform to geological features, enhancing resolution of potential anomaly boundaries at a higher computational cost. This visualization underscores the mesh's flexibility compared to the structured approach.

The computational workflow for inversion is established using a conjugate gradient least squares solver with zero-order Tikhonov regularization (regularization strength 1000, isotropic weighting factor 1.0). Traveltime tomography, governed by eikonal equations and solved through finite element methods, is utilized to reconstruct velocity models. Mesh quality, ray path coverage, and inversion accuracy are evaluated to compare the effectiveness of meshing strategies. The forward mesh quality is assessed in Fig. 4, confirming its adequacy through visualization of cell distribution and boundary conformity.

The computational workflow for inversion is established using a conjugate gradient least squares solver with zero-order Tikhonov regularization (regularization strength 1000, isotropic weighting factor 1.0). Traveltime tomography, governed by eikonal equations and solved through finite element methods, is utilized to reconstruct velocity models. Mesh quality, ray path coverage, and inversion accuracy are evaluated to compare the effectiveness of meshing strategies. The forward mesh quality is assessed in Fig. 4, confirming its adequacy through visualization of cell distribution and boundary conformity.

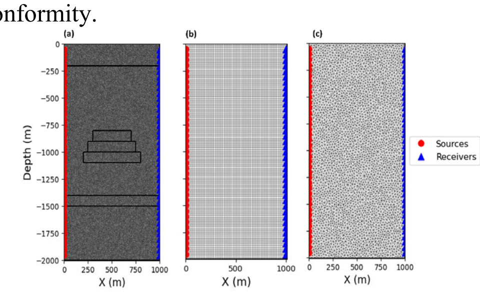

Fig. 3. (a) Geometric framework of the forward modeling mesh, delineating the subsurface discretization for wave propagation across the survey domain; (b) Structured inversion mesh configuration, illustrating a uniform grid-based discretization optimized for inversion stability; (c) Unstructured inversion mesh layout, showcasing an adaptive triangular discretization tailored to enhance resolution of subsurface features.

4. Results and Discussion

The efficacy of structured and unstructured meshing strategies in crosswell traveltime tomography is assessed through inversion results for a synthetic oil field model. An initial model, derived from borehole well logs, is utilized, incorporating layered velocities but excluding gas, oil, and saline water anomalies due to the absence of data from the central region. The reference apparent velocity matrix, obtained from forward simulations with 1521 source-receiver pairs, is visualized in Fig. 5a, establishing a benchmark for evaluating inversion performance across the general domain.

Apparent velocities predicted by the structured mesh inversion are presented in Fig. 5b. A uniform rectangular grid generates a smooth velocity field, but resolution of localized anomalies is constrained by the grid's rigidity. This uniform structure ensures computational stability but compromises the delineation of sharp velocity contrasts, particularly in heterogeneous regions.

In contrast, apparent velocities from the unstructured mesh inversion are depicted in Fig. 5c. Adaptive triangular discretization enhances the capture of velocity perturbations associated with anomalies, demonstrating superior sensitivity to subsurface complexity. This adaptability results in a closer alignment with the reference velocities, highlighting the unstructured mesh's effectiveness for detailed imaging.

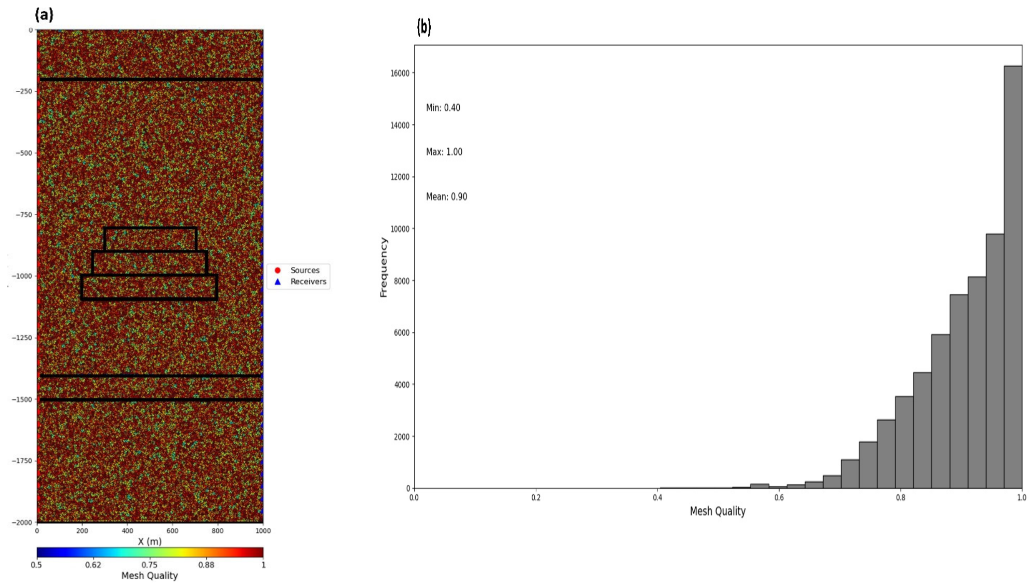

Fig. 4. (a) Spatial distribution of mesh quality across the forward model, overlaid with sensor and anomaly locations, highlighting variations in triangular element integrity within the survey domain; (b) Frequency distribution of mesh quality values, accompanied by statistical summaries, providing insight into the mesh's geometric consistency and encompassing insets showcasing the minimum, maximum, and the mean of the mesh quality values.

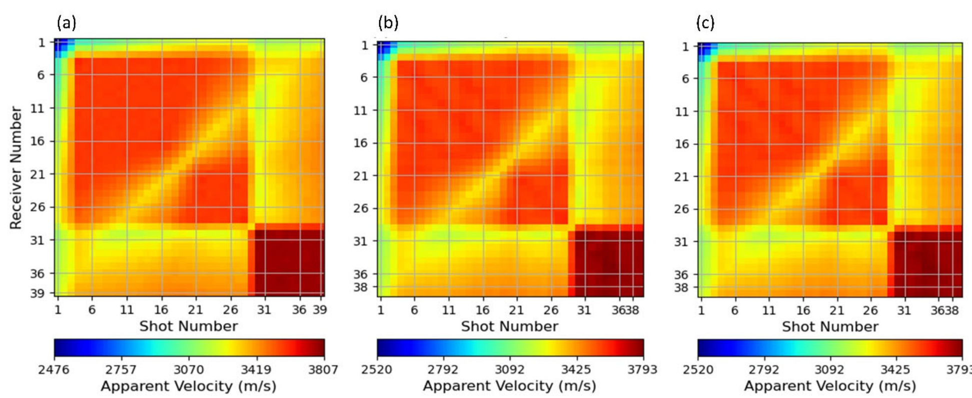

Fig. 5. (a) Matrix representation of apparent velocities derived from the forward simulation, reflecting the initial subsurface response across source-receiver pairs; (b) Matrix of apparent velocities predicted by the structured mesh inversion, illustrating the reconstructed response following uniform grid-based optimization; (c) Matrix of apparent velocities predicted by the unstructured mesh inversion, demonstrating the reconstructed response enhanced by adaptive triangular discretization.

Traveltime misfit for the structured mesh inversion is illustrated in Fig. 6a. Discrepancies across all source-receiver pairs are distributed uniformly, reflecting the grid's consistent but generalized approach. A χ_N^2 value of 2.16 (Table 3) indicates an acceptable fit, yet elevated misfits near anomaly boundaries suggest challenges in resolving localized variations, limiting precision in heterogeneous zones.

The misfit for the unstructured mesh inversion is shown in Fig. 6b. Reduced discrepancies are observed in regions of velocity transitions and anomalies, with a χ_N^2 of 1.72 and dφ of 1.35% (Table 3). This improved fit underscores the unstructured mesh's ability to adapt to subsurface heterogeneity, enhancing accuracy in critical areas and supporting reliable velocity reconstruction for oil field applications.

Table. 3. Post-Inversion Parameters.

Utilized Mesh type for Inversion	Structured Mesh-Based Inversion	Unstructured Mesh-Based Inversion
Number of Iterations	19	20
Runtime (S)	8417.34	3555.01
$\boldsymbol{\chi_N^2}$	2.16	1.72
$\boldsymbol{d\varphi}$ **(%)**	1.95	1.35
RMSE (%)	1.75	1.13
$\boldsymbol{\chi_N^2}$ **Improvement (%)**	-	20.37
$\boldsymbol{d\varphi}$ **Improvement (%)**	-	30.77
Runtime Improvement (%)	-	35.45
RMSE Improvement (%)	-	35.43

The reference velocity distribution, visualized in Fig. 7a, is overlaid with the forward modeling mesh. This benchmark confirms the accuracy of the synthetic traveltime data, providing a standard for assessing the fidelity of inversion-derived velocity models in capturing subsurface features.

The reconstructed velocity profile from the structured mesh inversion is presented in Fig. 7b. Major velocity transitions are reproduced, but anomalies are smoothed due to the uniform grid's limitations. This results in a generalized velocity field, less effective for resolving fine-scale heterogeneities critical for oil field characterization.

The unstructured mesh inversion's velocity profile is depicted in Fig. 7c. Precise delineation of anomaly boundaries and velocity contrasts is achieved, closely matching the reference model. The adaptive triangulation enhances resolution of localized features, making it well-suited for imaging complex subsurface structures in geophysical studies.

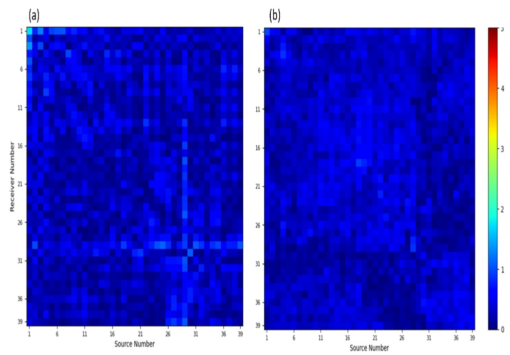

Fig. 6. (a) Misfit matrix depicting the relative traveltime discrepancies (in percentage) between observed and predicted data for the structured mesh inversion, highlighting inversion precision across source-receiver pairs; (b) Misfit matrix illustrating relative traveltime discrepancies for the unstructured mesh inversion, providing a comparative evaluation of adaptive discretization accuracy.

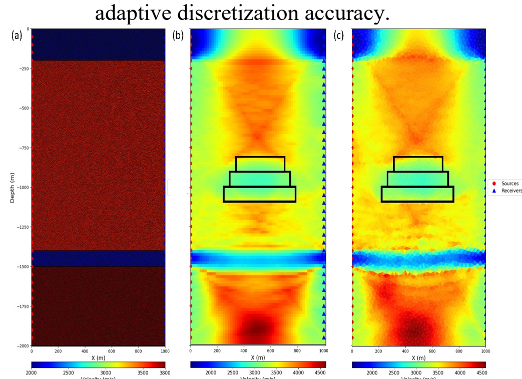

Fig. 7. (a) Reference subsurface velocity distribution overlaid with the forward modeling mesh, delineating the initial layered structure within the survey domain; (b) Reconstructed velocity profile derived from the structured mesh inversion, showcasing the impact of uniform discretization; (c) Reconstructed velocity profile from the unstructured mesh inversion, highlighting the influence of adaptive triangular discretization on subsurface imaging.

The structured mesh-based inversion ray path trajectories are illustrated in Fig. 8a. Uniform coverage across the domain is observed, consistent with the regular grid's structure. However, sparse ray density near anomaly interfaces reduces sensitivity to localized velocity changes, impacting the inversion's ability to resolve fine-scale features.

Ray path trajectories for the unstructured mesh inversion are shown in Fig. 8b. Increased ray density near anomaly boundaries is facilitated by adaptive triangulation. This enhanced coverage improves the reconstruction of velocity perturbations, reinforcing the unstructured mesh's advantage in capturing subsurface complexity for accurate imaging.

Ray path coverage for the structured mesh inversion is analyzed in Fig. 9a. A consistent but sparse distribution is observed, reflecting the uniform grid's limitations in resolving localized variations. This reduced coverage contributes to higher misfits in heterogeneous regions, as indicated by the χ_N^2 value.

The ray path coverage for the unstructured mesh inversion is presented in Fig. 9b. Elevated ray density in anomaly regions enhances resolution of velocity contrasts, corroborated by the lower χ_N^2 and dφ. This improved coverage supports precise imaging, highlighting the unstructured mesh's superiority for complex subsurface structures.

In real-world crosswell tomography, challenges such as incomplete ray coverage, elevated signal noise, and geometry uncertainties often lead to increased χ_N^2 values, indicating larger data misfits compared to synthetic simulations. Unstructured meshing, with its adaptive triangular discretization (three nodes per cell), typically reduces inversion time compared to structured meshing, as it efficiently captures complex subsurface geometries with fewer computational nodes, enhancing boundary detection and resolution of velocity contrasts. However, achieving optimal results requires precise selection of inversion parameters, such as regularization strength and weighting factors, tailored to region-specific geological and petrophysical data to mitigate artifacts from noisy or sparse datasets. Unstructured meshes also better accommodate irregular ray paths and heterogeneous velocity fields, improving robustness in complex field conditions, though they demand careful mesh quality control to avoid numerical instability. In contrast, structured meshes provide computational stability but may oversmooth anomalies in noisy environments, compromising fine-scale feature resolution. Field validations integrating region-specific prior models and adaptive regularization could further refine these meshing strategies for practical oil field applications.

In shallow subsurface investigations with high-velocity-gradient environments, such as those in mining or geotechnical applications, seismic crosswell tomography faces challenges from abrupt velocity changes and complex geological boundaries. Unstructured meshing, with its adaptive triangulation, excels at resolving sharp velocity contrasts and small-scale features like faults, mirroring its effectiveness in deep hydrocarbon settings, while its efficiency is enhanced in smaller domains due to reduced node counts. Structured meshing, though computationally stable, may oversmooth rapid velocity transitions, limiting resolution in heterogeneous zones. Optimal meshing requires tailoring inversion parameters to site-specific velocity and data characteristics to minimize artifacts. Field validations in shallow contexts could confirm these findings, potentially exploring hybrid meshing for balanced performance.

A hybrid meshing approach, with finer resolution at anomaly locations and coarser meshing elsewhere, could enhance hydrocarbon trap boundary delineation by leveraging the adaptive resolution of unstructured meshes and the stability of structured meshes, provided sufficient computational power is available. Weighted integration of inversion results is less applicable here, however, for the time when real field data is being used and the ambiguity in inversion results is high, this kind of integration can be useful. Future studies could validate hybrid meshing's effectiveness for trap boundary imaging in synthetic and field datasets, contingent on computational resources.

as

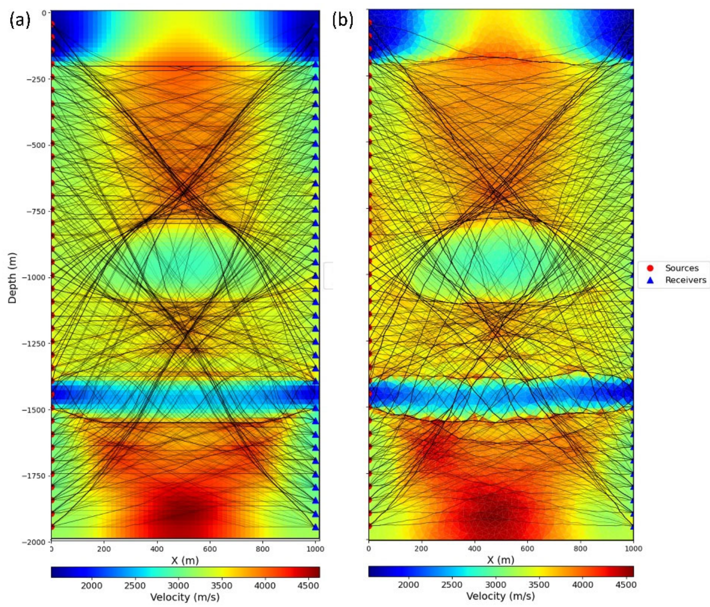

Fig. 8. (a) Reconstructed subsurface velocity profile from the structured mesh inversion, enhanced with overlaid ray path trajectories to indicate data coverage; (b) Reconstructed subsurface velocity profile from the unstructured mesh inversion, supplemented with ray path trajectories to assess the adaptive discretization's influence on imaging accuracy.

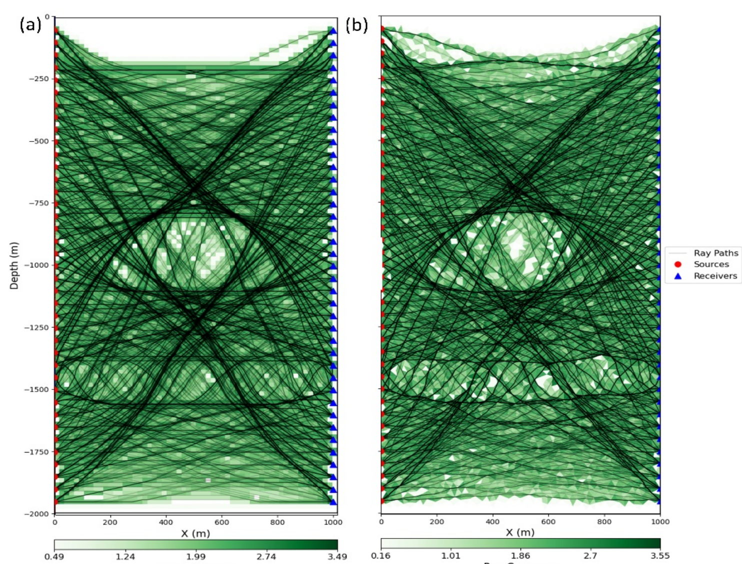

Fig. 9. (a) Spatial distribution of ray path coverage for the structured mesh inversion, illustrating data sensitivity across the domain; (b) Corresponding coverage distribution for the unstructured mesh inversion, providing a comparative assessment of mesh influence on resolution.

The inversion results are sensitive to parameters such as regularization strength (λ = 1000), mesh resolution, and noise level, significantly influencing velocity model accuracy in crosswell traveltime tomography. The choice of λ = 1000 was determined to balance data misfit and model smoothness, ensuring stable convergence for the synthetic model's noise levels (0.1% relative, 10^{-5} s absolute) and layered structure with anomalies, further necessitated by the large and deep modeling domain (2000 m) to stabilize the inversion. Higher regularization may overly smooth velocity contrasts, particularly in structured meshes, while lower values risk noise amplification in unstructured meshes with finer resolution. Coarser mesh resolutions reduce computational cost but blur anomaly boundaries, whereas finer meshes enhance detail at increased computational expense. Elevated noise levels beyond the simulated values can degrade model fidelity, especially for structured meshes in heterogeneous regions. Iterative tuning of these parameters, guided by data quality and geological complexity, optimizes inversion outcomes. However, this study's reliance on synthetic 2D modeling, without field validation or 3D modeling, limits direct applicability to real-world settings, necessitating further research to confirm these findings in complex field conditions. Meshing parameters (Table 2) and post-inversion metrics (Table 3) provide critical insights into the trade-offs between meshing strategies. As shown in Table 3, the unstructured mesh inversion (6620 cells) requires 4684.20 s, a 35.45% improvement over the 7256.62 s for the structured mesh (6612 cells), despite a similar cell count, highlighting superior computational efficiency. Furthermore, Table 3 indicates that the unstructured mesh achieves a lower χ_N^2 (1.72 vs. 2.16, a 20.37% improvement), dφ (1.35% vs. 1.95%, a 30.77% improvement), and RMSE (1.13% vs. 1.75%, a 35.43% improvement), demonstrating faster convergence and better fit to the observed data. These results underscore the unstructured mesh's advantages in resolution and efficiency, making it preferable for detailed subsurface characterization in crosswell tomography, with implications for optimizing geophysical imaging in oil field exploration.

Aftab et al. [40] utilized pyGIMLi to study the effects of anomaly number, dimensions, and location in 2D crosswell traveltime tomography, achieving low inversion errors for anomaly detection in synthetic models. In contrast, this study applies pyGIMLi to a deeper 2000 m medium with a realistic geological scenario, comparing structured and unstructured meshing to enhance resolution and efficiency, addressing a timely oil field characterization challenge.

5. Conclusion

The performance of structured and unstructured meshing strategies in crosswell traveltime tomography is evaluated, revealing the pivotal influence of mesh design on subsurface velocity Unstructured meshing reduces χ_N^2 from 2.16 to 1.72 (20.37% improvement), dφ from 1.95% to 1.35% (30.77% improvement), and relative RMSE from 1.75% to 1.13% (35.43% improvement), while cutting inversion time from 8417.34 s to 3555.01 s (35.45% improvement). These quantitative improvements demonstrate superior accuracy and computational efficiency for crosswell tomography in complex geological settings. Adaptive meshing is demonstrated to significantly enhance the resolution of complex geological features, including localized velocity perturbations, thereby improving imaging precision in heterogeneous subsurface environments. In contrast, uniform meshing is found to offer computational stability and efficiency, making it well-suited for simpler geological settings where fine-scale resolution is less critical. These insights, derived from comparative analysis, are established to guide the optimization of tomographic inversion techniques, enabling geophysical practitioners to make informed decisions when balancing imaging accuracy with computational resources. The study's findings are recognized as a contribution to advancing non-invasive subsurface imaging, supporting the development of robust methodologies for resource exploration and reservoir management. Future research directions are proposed, including the exploration of hybrid meshing frameworks and extension to 3D domains, to validate the synthetic 2D findings of this study through field data and address limitations in real-world applicability. Additionally, the extension of these methods to three-dimensional domains is suggested to address more realistic geological complexities. The incorporation of advanced regularization strategies or machine learning-assisted inversion is also recommended to enhance the robustness of crosswell tomography across diverse subsurface contexts. This work is positioned as a foundation for ongoing efforts to improve geophysical imaging, fostering innovations that enhance the efficiency and accuracy of subsurface characterization in oil field applications.

3. Acknowledgment

We are deeply grateful to the School of Mining Engineering at the University of Tehran for their unwavering support and assistance.

4. References

.[1] C. Zhou, W. Cai, Y. Luo, G. Schuster, and S. Hassanzadeh, "High-resolution cross-well imaging by seismic traveltime + waveform inversion," The Leading Edge, vol. 12, no. 10, pp. 988–993, Oct. 1993, doi: 10.1190/1.1436918.

[2] G. G. Leiceaga, B. Marion, K. M. O'Sullivan, G. Bunge, J. T. Nielsen, and A. Fryer, "Crosswell seismic applications for improved reservoir understanding," The Leading Edge, vol. 34, no. 4, pp. 422–428, Apr. 2015, doi: 10.1190/tle34040422.

[3] R. G. Pratt, L. Sirgue, B. Hornby, and J. Wolfe, "Crosswell Waveform Tomography in Fine-layered Sediments - Meeting the Challenges of Anisotropy," in 70th EAGE Conference and Exhibition incorporating SPE EUROPEC 2008, European Association of Geoscientists & Engineers, 2008. doi: 10.3997/2214-4609.20147681.

[4] D. Cao and W. Liao, "An Adjoint-Based Hybrid Computational Method for Crosswell Seismic Inversion," Comput Sci Eng, vol. 16, no. 6, pp. 60–67, Nov. 2014, doi: 10.1109/MCSE.2014.

[5] J. Liao et al., "Application of Frequency-Dependent Traveltime Tomography to 2D Crosswell Seismic Field Data," J Environ Eng Geophys, vol. 22, no. 4, pp. 421–426, Dec. 2017, doi: 10.2113/JEEG22.4.421.

[6] C. Li, J. Liu, J. Liao, and A. Hursthouse, "2D High-Resolution Crosswell Seismic Traveltime Tomography," J Environ Eng Geophys, vol. 25, no. 1, pp. 47–53, Mar. 2020, doi: 10.2113/JEEG19-003.

[7] A. V. Chugaev, I. A. Sanfirov, and M. V. Tarantin, "Cross-Well Reflection Imaging at the Verkhnekamskoe Potash Deposit," Russian Geology and Geophysics, vol. 64, no. 2, pp. 243–255, Feb. 2023, doi: 10.2113/RGG20214406.

[8] Z. R. Wei, F.-L. Yang, B.-H. Liu, and Y.-L. Pei, "Inverse Gaussian-beam common-reflection-point-stack imaging in crosswell seismic tomography," Applied Geophysics, vol. 16, no. 3, pp. 349–357, Sep. 2019, doi: 10.1007/s11770-019-0768-z.

[9] F.-L. Yang et al., "Inverse gaussian beam stack imaging in 3D crosswell seismic exploration of deviated wells and Its application," Applied Geophysics, vol. 17, no. 5–6, pp. 629–638, Dec. 2020, doi: 10.1007/s11770-019-0830.

[10] F.-L. Yang, G.-Y. Ren, F.-M. Yao, and C. Zhao, "The Inverse Fresnel Beam XSP-CDP Stack Imaging in Crosswell Seismic," Front Earth Sci (Lausanne), vol. 10, Mar. 2022, doi: 10.3389/feart.2022.851379.

[11] J. Yang, X. He, and H. Chen, "Crosswell frequency-domain reverse time migration imaging with wavefield decomposition," Journal of Geophysics and Engineering, vol. 20, no. 6, pp. 1279–1290, Oct. 2023, doi: 10.1093/jge/gxad083.

[12] T. Zhu and J. M. Harris, "Improved seismic image by Q -compensated reverse time migration: Application to crosswell field data, west Texas," GEOPHYSICS, vol. 80, no. 2, pp. B61–B67, Mar. 2015, doi: 10.1190/geo2014-0463.

[13] R. R. S. Dantas and W. E. Medeiros, "Resolution in crosswell traveltime tomography: The dependence on

illumination," GEOPHYSICS, vol. 81, no. 1, pp. W1–W12, Jan. 2016, doi: 10.1190/geo2015-0119.

[14] T. Suroso, H. Laksono, W. Triyoso, and A. Priyono, "Estimating anisotropy parameter by shear wave splitting of crosswell seismic data: a case study on inter-bedded sand-shale layers," IOP Conf Ser Earth Environ Sci, vol. 62, p. 012019, Apr. 2017, doi: 10.1088/1755-1315/62/1/012019.

[15] M. A. C. Tura, R. J. Greaves, and W. B. Beydoun, "Crosswell seismic reflection/diffraction tomography: A reservoir characterization application," GEOPHYSICS, vol. 59, no. 3, pp. 351–361, Mar. 1994, doi: 10.1190/1.1443597.

[16] A. F. Marsala et al., "Saturation Mapping in the Interwell Reservoir Volume: A New Technology Breakthrough," in SPE Annual Technical Conference and Exhibition, SPE, Oct. 2017. doi: 10.2118/187371-MS.

[17] D. Zang, Y. Ji, Y. Chao, and Z. Li, "Signal processing methods for crosswell electromagnetic imaging system," Interpretation, vol. 11, no. 1, pp. T171–T180, Feb. 2023, doi: 10.1190/INT-2021-0157.

[18] K. Katterbauer, I. Hoteit, and S. Sun, "Synergizing Crosswell Seismic and Electromagnetic Techniques for Enhancing Reservoir Characterization," SPE Journal, vol. 21, no. 03, pp. 909–927, Jun. 2016, doi: 10.2118/174559.

[19] M. Commer, J. Doetsch, B. Dafflon, Y. Wu, T. M. Daley, and S. S. Hubbard, "Time-lapse 3-D electrical resistance tomography inversion for crosswell monitoring of dissolved and supercritical CO2 flow at two field sites: Escatawpa and Cranfield, Mississippi, USA," International Journal of Greenhouse Gas Control, vol. 49, pp. 297–311, Jun. 2016, doi: 10.1016/j.ijggc.2016.03.020.

[20] A. R. Rahmani et al., "Crosswell Magnetic Sensing of Superparamagnetic Nanoparticles for Subsurface Applications," SPE Journal, vol. 20, no. 05, pp. 1067–1082, Oct. 2015, doi: 10.2118/166140.

[21] G. Böhm, J. M. Carcione, D. Gei, S. Picotti, and A. Michelini, "Cross-well seismic and electromagnetic tomography for CO2 detection and monitoring in a saline aquifer," J Pet Sci Eng, vol. 133, pp. 245–257, Sep. 2015, doi: 10.1016/j.petrol.2015.06.010.

[22] Y. Zhang, J. Fu, S. Jia, and J. Meng, "Application of Electrical Resistivity Tomography Method Combined with Cross-Well Seismic Computed Tomography Method in Karst Detection in Complex Urban Environment," Applied Sciences, vol. 15, no. 10, p. 5756, May 2025, doi: 10.3390/app15105756.

[23] D. Rampton and M. Small, "Evaluating an Unconventional Shale Completion with Repeat Crosswell Tomography," First Break, vol. 40, no. 1, pp. 67–73, Jan. 2022, doi: 10.3997/1365-2397.fb2022005.

[24] D. Rampton and M. J. Small, "Assessment of hydraulic fracture height and distribution using timelapse crosswell shear-wave data," J Appl Geophy, vol. 226, p. 105399, Jul. 2024, doi: 10.1016/j.jappgeo.2024.105399.

[25] J. Yu, J. Byun, and S. J. Seol, "VP/VS monitoring of CO2 sequestration using virtual horizontal crosswell tomography," Geosciences Journal, vol. 19, no. 3, pp. 441–448, Sep. 2015, doi: 10.1007/s12303-014-0053-3.

[26] N. Nakata, R. Nakata, A. Kato, Z. Xue, and M. C. A. White, "Enigmatic doubly scattered tube waves at a crosswell seismic survey," Geophys J Int, vol. 233, no. 1, pp. 627–640, Nov. 2022, doi: 10.1093/gji/ggac471.

[27] J. Zhang and A. Revil, "Cross-well 4-D

resistivity tomography localizes the oil–water encroachment front during water flooding," Geophys J Int, vol. 201, no. 1, pp. 343–354, Apr. 2015, doi: 10.1093/gji/ggv028.

[28] M. Commer et al., "An adaptable technique for comparative image assessment: Application to crosswell electromagnetic survey design for fluid monitoring," GEOPHYSICS, vol. 86, no. 3, pp. E239–E256, May 2021, doi: 10.1190/geo2020-0430.

[29] T. Yamamoto, T. Nye, and M. Kuru, "Porosity, permeability, shear strength: Crosswell tomography below an iron foundry," GEOPHYSICS, vol. 59, no. 10, pp. 1530–1541, Oct. 1994, doi: 10.1190/1.1443542.

[30] J. E. Peterson and A. Davey, "Crossvalidation method for crosswell seismic tomography," GEOPHYSICS, vol. 56, no. 3, pp. 385–389, Mar. 1991, doi: 10.1190/1.1443055.

[31] A. Rüger and D. Hale, "Meshing for velocity modeling and ray tracing in complex velocity fields," GEOPHYSICS, vol. 71, no. 1, pp. U1–U11, Jan. 2006, doi: 10.1190/1.2159061.

[32] C. Pelties, M. Käser, V. Hermann, and C. E. Castro, "Regular versus irregular meshing for complicated models and their effect on synthetic seismograms," Geophys J Int, vol. 183, no. 2, pp. 1031–1051, Nov. 2010, doi: 10.1111/j.1365-246X.2010.04777.

[33] R. Cockett, S. Kang, L. J. Heagy, A. Pidlisecky, and D. W. Oldenburg, "SimPEG: An open source framework for simulation and gradient based parameter estimation in geophysical applications," Comput Geosci, vol. 85, pp. 142–154, Dec. 2015, doi: 10.1016/J.CAGEO.2015.09.015.

[34] C. Rücker, T. Günther, and F. M. Wagner, "pyGIMLi: An open-source library for modelling and inversion in geophysics," Comput Geosci, vol. 109, pp. 106–123, Dec. 2017, doi: 10.1016/j.cageo.2017.07.011.

[35] F.-C. Lin, M. H. Ritzwoller, and R. Snieder, "Eikonal tomography: surface wave tomography by phase front tracking across a regional broad-band seismic array," Geophys J Int, vol. 177, no. 3, pp. 1091–1110, Jun. 2009, doi: 10.1111/j.1365-246X.2009.04105.

[36] A. Yazdanpanah and M. Abedi, "Geophysical simulation of landslide model based on electrical resistivity and refraction seismic tomography through unstructured meshing," International Journal of Mining and Geo-Engineering, vol. 58, no. 3, pp. 263–270, 2024, doi: 10.22059/ijmge.2024.370406.595136

[37] D. A. Field, "Qualitative measures for initial meshes," Int J Numer Methods Eng, vol. 47, no. 4, pp. 887–906, Feb. 2000.

[38] M. S. Zhdanov, G. Vignoli, and T. Ueda, "Sharp boundary inversion in crosswell travel-time tomography," Journal of Geophysics and Engineering, vol. 3, no. 2, pp. 122–134, Jun. 2006, doi: 10.1088/1742-2132/3/2/003.

[39] D. W. Oldenburg and Y. Li, "INVERSION FOR APPLIED GEOPHYSICS: A TUTORIAL," 2005.

[40] S. Aftab, R. H. Moghadam, and A. Leisi, "The effect of the number, dimensions and location of anomalies on the crosswell Traveltime tomography results," 5133, doi: 10.22107/JPG.2023.384315.1187.